Sensors and Actuators A 155 (2009) 217–225

Contents lists available at ScienceDirect

Sensors and Actuators A: Physical

journal homepage: www.elsevier.com/locate/sna

Critical challenges for picoTesla magnetic-tunnel-junction sensors☆

W.F. Egelhoff Jr. [a], P.W.T. Pong [a,*], J. Unguris [b], R.D. McMichael [b], E.R. Nowak [c], A.S. Edelstein [d], J.E. Burnette [d], G.A. Fischer [d]

[a] Metallurgy Division, National Institute of Standards & Technology, Gaithersburg, MD 20899-8552, United States
[b] Center for Nanoscale Science and Technology, National Institute of Standards & Technology, Gaithersburg, MD 20899-8552, United States
[c] Department of Physics and Astronomy, University of Delaware, Newark, DE 19716, United States
[d] U.S. Army Research Laboratory, Adelphi, MD 20783-1197, United States

ARTICLE INFO

Article history:
Received 7 April 2009
Received in revised form 24 August 2009
Accepted 26 August 2009
Available online 2 September 2009

Keywords:
picoTesla
Magnetic-tunnel-junction
Magnetic sensors
Tunneling magnetoresistance

ABSTRACT

The extension of small, inexpensive, low-power, low-frequency, ultra-sensitive magnetic sensors to fields between 1 nT and 1 pT, an area currently dominated by fluxgates, optically pumped magnetometers, and SQUIDS, would be a paradigm shift for the field of magnetic sensors. The necessary elements for picoTesla magnetic-tunnel-junction (MTJ) sensors have been identified by modeling the noise characteristics. The results help identify the experimental challenges involved in the integration of these necessary elements into actual sensors, illustrate the trade-offs faced if there are losses in performance upon integration. Scanning electron microscopy with polarization analysis (SEMPA) of the pinned layer provides insights into problems and possible solutions. Issues associated with real-world applications of these sensors to ultra-low field measurements are discussed.

1. Introduction

The number of applications for magnetic sensors has grown explosively in the past two decades [1]. In particular, the growth in small, low-power magnetic sensors has been exponential [2]. Applications abound to meet the needs of users in the medical, military, information technology, and industrial communities [3]. However, one area in which little progress has been made in recent years is small, inexpensive, low-power low-frequency sensors capable of detecting ultra-low magnetic fields. By small we mean sub-millimeter. By inexpensive we mean a few tens-of-dollars each. By low-power we mean the sensor elements consume a few milliWatts or less. By low frequency we mean approximately 0.01 Hz to 100 Hz. Currently, the detection of fields between 1 nT (10^{-5} Oe) and 1 pT (10^{-8} Oe) is dominated by relative large, expensive, power-hungry sensors such as fluxgates, optically pumped magnetometers and SQUIDs [4]. If small, inexpensive, low-power, low-frequency magnetic sensors could make serious progress in this regime the technological impact would likely be great [4].

The most likely sensor technology to make such progress is a Wheatstone bridge of magnetic-tunnel-junctions (MTJs) combined with a micro-electro-mechanical system (MEMS) of frequency-modulated magnetic flux concentrators to suppress $1/f$ noise [5,6]. An important aspect of this approach is that magnetic flux concentrators do not contribute significantly to $1/f$ noise [5]. To evaluate the combined effect of this approach, a theoretical model was derived and incorporated in a spreadsheet for evaluation and optimization of the expected performance of the sensor.

2. Theoretical model

The sensor design has N MTJs in each leg of a Wheatstone bridge. On each side of the bridge one leg of MTJs is shielded from the applied magnetic field and one is exposed (Fig. 1a). The applied field is amplified by MEMS flux concentrators that provide a field gain β [6].

2.1. Performance

When the resistance of the two active legs changes by δR, the output voltage of the bridge is

$$V = Vo\frac{\delta R}{2R+\delta R} \approx V_0\frac{\delta R}{2R} \quad (1)$$

Here V_0 is the supply voltage and R is the resistance of one leg of the bridge. The sensitivity of the bridge is determined by the

☆ Disclaimer: The identification of a commercial software and sensors is to specify the experimental conditions and does not imply any NIST endorsement or recommendation that it is necessarily the best for the purpose.

* Corresponding author. Present address: Department of Electrical and Electronic Engineering, University of Hong Kong, Pokfulam Road, Hong Kong.
E-mail address: ppong@eee.hku.hk (P.W.T. Pong).

0924-4247/$ – see front matter © 2009 Published by Elsevier B.V.
doi:10.1016/j.sna.2009.08.016

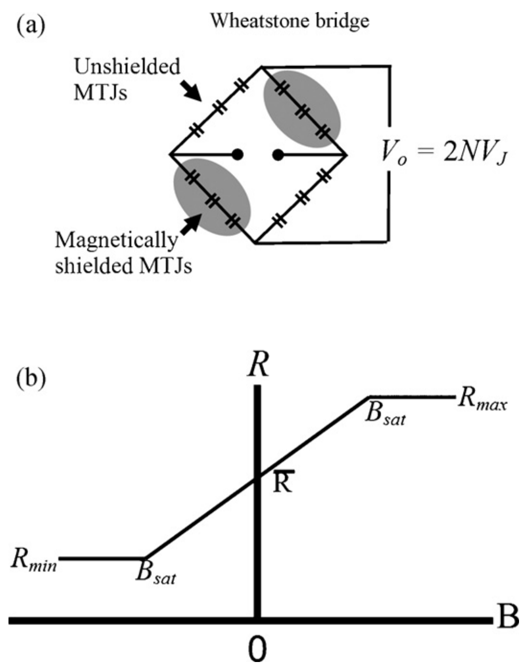

Fig. 1. A definition of the terms used in modeling a) the Wheatstone bridge sensor and b) in modeling the plot of resistance versus field of the MTJ response in Eqs. (1)–(3).

change in resistance due to the applied field. For an applied field B, and assuming a linear response, the resistance changes by

$$\delta R = \frac{R_{\max} - R_{\min}}{2} \frac{B}{B_{\text{sat}}} \tag{2}$$

The sensitivity of the bridge is therefore

$$\frac{dV}{dB} = \frac{\Delta R}{\bar{R}} \frac{V_0}{4B_{\text{sat}}} \tag{3}$$

Note that the fraction $\Delta R/\bar{R}$ is explicitly, $2(R_{\max} - R_{\min})/(R_{\max} + R_{\min})$, which is different from the value usually published, $(R_{\max} - R_{\min})/R_{\min}$ (Fig. 1b). It may be more convenient for design purposes to write the supply voltage in terms of the junction voltage $V_J = V_0/2N$, where N is the number of MTJs per leg.

$$\frac{dV}{dB} = \frac{\Delta R}{\bar{R}} \frac{NV_J}{2B_{\text{sat}}} \tag{4}$$

The overall power dissipated by the device is

$$W = 4N \frac{V_J^2 A}{[RAP]} \tag{5}$$

where A is the area of each MTJ and [RAP] is the resistance-area product. In this analysis, the junction voltage V_J, the junction area A and the number of MTJs per leg N are used as design parameters for the bridge circuit. Other quantities are expressed in terms of these three, when possible.

2.2. Noise sources

For a Wheatstone bridge, the field noise power, S_B (units of T^2/Hz) at the output is equal to the noise in one leg, assuming that the four legs all have equivalent noise sources. The analysis below includes amplifier noise, Shot and Johnson noise, electronic $1/f$ noise, thermal magnetic noise, and magnetic $1/f$ noise [11,17–19]. The detection limit will be determined by a field noise floor

$$S_B = S_B^{\text{Amp}} + S_B^{\text{shot}} + S_B^{\text{elec.}1/f} + S_B^{\text{therm.mag.}} + S_B^{\text{mag.}1/f} \tag{6}$$

Table 1
A definition of the terms used in Eqs. (1)–(24).

N	Number of MTJs in each leg of the Wheatstone bridge
S_B	Sensor field noise power, T^2/Hz
B_{sat}	Saturation field of free layer, T
ΔR	Resistance change of one MTJ from parallel to antiparallel magnetization
$\bar{R}$	Resistance of one MTJ in orthogonal magnetization state
V_J	Voltage drop across each MTJ
V_0	The supply voltage, $2NV_J$
S_V^{amp}	Amplifier noise voltage power
S_V^{shot}	Shot-noise voltage power
$S_V^{\text{elec.}1/f}$	Electronic $1/f$ noise voltage power
$S_M^{\text{therm.mag.}}$	Thermal-magnetic noise magnetization power
$S_V^{\text{therm.mag.}}$	Thermal-magnetic noise voltage power
$S_B^{\text{therm.mag.}}$	Thermal-magnetic noise field power
$S_M^{\text{mag.}1/f}$	Magnetic $1/f$ noise magnetization power of one MTJ
$S_V^{\text{mag.}1/f}$	Magnetic $1/f$ noise voltage power of one MTJ
$S_B^{\text{mag.}1/f}$	Magnetic $1/f$ noise field power of a bridge
e	Electronic charge
RAP	Resistance-area product of each MTJ
A	Area of each MTJ
k_B	Boltzmann's constant
T	Absolute temperature
α_{elect}	Electronic $1/f$ Hooge parameter
α_{mag}	Magnetic $1/f$ Hooge parameter
f	Frequency of operation of MEMS flux concentrator
μ_0	Permeability of free space
α_G	Gilbert damping parameter
Ω	Free-layer volume in each MTJ
γ	Gyromagnetic ratio for an electron
M_s	Saturation magnetization of the free layer per unit volume

2.2.1. Amplifier noise

An amplifier connected to the output of the bridge will have internal noise that will limit the field noise power floor. The amplifier noise level can be expressed as noise voltage power S_V^{Amp} in units of $[V^2/\text{Hz}]$. The effective noise field power due to the amplifier noise is given by

$$S_B^{\text{Amp}} = \left(\frac{dB}{dV}\right)^2 S_V^{\text{Amp}} \tag{7}$$

where dB/dV is the inverse of Eq. (4).

For convenience, all parameters are defined in Table 1.

2.2.2. Shot and Johnson noise

Shot noise and Johnson noise are intertwined in tunnel junctions [7]. The general expression for this noise voltage power is

$$S_V^{\text{shot}} = N2eIR_J^2 \coth\left(\frac{eV_J}{2k_BT}\right) \tag{8}$$

Note that for small junction voltages, less than about 50 mV at room temperature, Eq. (8) reduces to $N4k_BT$, the expression for Johnson noise, because electron transport tends to be diffusive across the junction. At higher junction voltages, as current flow becomes unidirectional, Johnson noise fades away, and shot noise (the statistics of counting electrons) dominates. In terms of our design parameters, the junction resistance $R_J = [RAP]/A$ where $[RAP]$ is the resistance-area product and A is the area of each tunnel junction. The current is $I = 2NV_J/2NR_J$, and the junction voltage is $V_J = 2NV_J/2N$. In terms of the design parameters,

$$S_V^{\text{shot}} = N\frac{2eV_J[RAP]}{A} \coth\left(\frac{eV_J}{2k_BT}\right) \tag{9}$$

2.2.3. Electronic 1/f noise

The electronic 1/*f* noise voltage power (units of V^2/Hz) varies among MTJs, but it is typically written as [7]

$$S_V^{1/f} = N\frac{\alpha_{\mathrm{elect.}} I^2 R_J^2}{Af} \tag{10}$$

where *f* is the detection frequency and α_{elect}, the electronic Hooge parameter, acts as a constant of proportionality to enable modeling of the 1/*f* noise voltage power for differing values of *N*, V_J, *A*, and *f* in a bridge of MTJs. The prefactor of *N* results from the noise voltage (the square root of the noise voltage power) of the MTJs adding in quadrature so the noise voltage power of each MTJ in the leg adds linearly to give *N*. The same principle will apply to the next two types of noise in Sections 4 and 5 below.

Note the Hooge parameter may need to be recalculated for different MTJs, although trends in its value as a function of *RAP* have been noted for different MTJs [8]. In terms of our design parameters, the 1/*f* noise voltage power becomes

$$S_V^{1/f} = N\frac{\alpha_{\mathrm{elect.}} V_J^2}{Af} \tag{11}$$

2.2.4. Thermal magnetic noise

The thermal fluctuations of the free-layer magnetization will contribute to sensor noise. The thermal magnetic noise power for a single junction is given by

$$S_M^{\mathrm{therm.mag.}} = \frac{2k_B T\chi''(f)}{\pi\Omega\mu_0 f} \tag{12}$$

where Ω is the free-layer volume [9]. The imaginary part of the susceptibility, $\chi''(f)$ is usually thought of as the coefficient that describes losses driven by applied fields. In this context, it describes how the thermal bath couples to the magnetization. At least two mechanisms may contribute to $\chi''(f)$, including uniform rotation of the free-layer magnetization and metastability of ripple states. The part attributable to uniform rotation is generally referred to as thermal magnetic noise. The part attributable to ripple is generally referred to as magnetic 1/*f* noise.

Since here we consider frequencies far below ferromagnetic resonance, we can write for the free-layer uniform-rotation mechanism,

$$\chi'' = \frac{\alpha_G M_s \omega}{\gamma H_k^2} \tag{13}$$

Here we give the Gilbert damping parameter α_G a subscript to separate it from the Hooge parameters, and H_k is the in-plane stiffness field of the magnetization. For susceptibility due to magnetization rotation, the magnetization noise power is [9]

$$S_M^{\mathrm{therm.mag.}} = \frac{4k_B T\alpha_G M_s \mu_0}{\Omega\gamma B_{\mathrm{sat}}^2} \tag{14}$$

The output noise voltage power due to the magnetization fluctuations of the free-layer rotation is given by

$$S_V^{\mathrm{therm.mag.}} = N\left(\frac{dV_J}{dM}\right)^2 S_M^{\mathrm{therm.mag.}} = N\left(\frac{V_J(\Delta R/\bar{R})}{2M_s}\right)^2 S_M^{\mathrm{therm.mag.}} \tag{15}$$

and using the inverse of Eq. (4) to calculate the effective field noise power due to magnetization fluctuations [9]

$$S_B^{\mathrm{therm.mag.}} = \left(\frac{dB}{dV}\right)^2 S_V^{\mathrm{therm.mag.}} = \frac{1}{N}\frac{4k_B T\mu_0\alpha_G}{\Omega\gamma M_s} \tag{16}$$

2.2.5. Magnetic 1/f noise

The other mechanism that will contribute to χ'' is magnetization hopping between metastable ripple states [5,10]. Since there will be a distribution of energy barriers, there is a likelihood that this mechanism will lead to a 1/*f*-type noise, [5,10] or, if the density of these ripple-based flip-floppers is small, to telegraph noise. Using Eq. (12) to describe this mechanism, the lossy part of the susceptibility has a precessonal part given by Eq. (13), and a hysteretic part which is nearly frequency independent. Then summing the magnetic 1/*f* voltage noise power over the *N* MTJs in the bridge,

$$S_V^{\mathrm{mag.}1/f} = N\left(\frac{dV_J}{dM}\right)^2 S_M^{\mathrm{mag.}1/f} = N\left[\frac{V_J\,\Delta R/\bar{R}}{2M_s}\right]^2 \frac{2k_B T\chi''(f)}{\pi\Omega\mu_0 f} \tag{17}$$

The sensitivity of an MTJ is

$$\frac{dV}{dH} = \frac{dV}{dM}\frac{dM}{dH} = \frac{V_J\,\Delta R/\bar{R}}{2M_s}\chi' \tag{18}$$

where χ' is the real part of the susceptibility and V_J, ΔR, $\bar{R}$, and M_s are all constants independent of applied field. The only field-dependent quantities in Eqs. (17) and (18) are χ' and χ''. To a first approximation, χ' and χ'' are linearly related as a function of applied field (at least at low fields and low frequencies, *i.e.*, $<B_{\mathrm{sat}}$ and <10 kHz). Consequently, S_V and dV/dH are linearly related, as demonstrated in Ref. [8].

Then, $S_B^{\mathrm{mag.}1/f}$ becomes, from $S_V^{\mathrm{mag.}1/f}$,

$$S_B^{\mathrm{mag.}1/f} = \left(\frac{dB}{dV}\right)^2 S_V^{\mathrm{mag.}1/f} = N\left[\frac{2B_{\mathrm{sat}}}{NV_J\,\Delta R/\bar{R}}\right]^2\left[\frac{V_J\,\Delta R/\bar{R}}{2M_s}\right]^2\frac{2k_B T\chi''(f)}{\pi\Omega\mu_0 f} \tag{19}$$

$$= \frac{1}{N}\frac{2k_B T\chi''(f)}{\pi\Omega\mu_0 f}\left[\frac{B_{\mathrm{sat}}}{M_s}\right]^2 = \frac{1}{N}\frac{2k_B T\chi''(f)}{\pi\Omega f}\frac{H_{\mathrm{sat}}}{M_s}\frac{B_{\mathrm{sat}}}{M_s} \tag{20}$$

Recognizing that M_s/H_{sat} is our assumed model for χ',

$$S_B^{\mathrm{mag.}1/f} = \frac{1}{N}\frac{2k_B T}{\pi\Omega f}\left[\frac{\chi''}{\chi'}\right]\frac{B_{\mathrm{sat}}}{M_s} \quad \text{or} \quad \frac{2B_{\mathrm{sat}}}{N}\frac{\alpha_{\mathrm{mag}}}{\Omega f} \tag{21}$$

$$\text{with } \alpha_{\mathrm{mag}} = \frac{1}{N}\frac{k_B T}{\pi M s}\left[\frac{\chi''}{\chi'}\right] \tag{22}$$

and the quantity in parentheses is the fraction of the susceptibility that is irreversible. Note that the magnetic 1/*f* noise α_{mag} parameter, much like the above Hooge parameter, acts as a constant of proportionality to enable modeling of the magnetic 1/*f* noise field power for differing values of *N*, V_J, Ω, and *f* in a bridge of MTJs. The value we use for α_{mag} in our modeling is an experimental derived one $1.83 \times 10^{-12}\ \mu\mathrm{m}^3\ \mathrm{T}$ [12].

It is a critical distinction that an increase in MTJ sensitivity can overcome amplifier, Johnson, shot, and electronic 1/*f* noise but might not be expected to do so for magnetic 1/*f* noise. Magnetic 1/*f* noise represents fluctuations in the direction of the magnetization that might seem fundamentally indistinguishable from fluctuations caused by an external magnetic field that one wants to detect. It might appear that no amount of sensitivity would help the sensor distinguish a real external signal from magnetic 1/*f* noise. However, reality is more complex. The B_{sat} in Eq. (21) means that if MTJ sensitivity is increased by decreasing B_{sat}, the magnetic 1/*f* noise can be suppressed without limit. This result has practical consequences since the magnetic 1/*f* noise is often dominant, and Eq. (21) points to a new way to suppress it.

2.2.6. Total system noise

The grand total system field noise power is then given by

$$S_B = \left(\frac{dB}{dV}\right)^2\left[S_V^{\mathrm{Amp}} + S_V^{\mathrm{shot}} + S_V^{\mathrm{elec.}1/f}\right] + S_B^{\mathrm{therm.mag.}} + S_B^{\mathrm{mag.}1/f} \tag{23}$$

Table 2
A set of "best compromise" input parameters for Eq. (24) corresponding to reasonably achievable values for an MTJ-based sensor that would yield a noise floor of 1 pT/rt(Hz). Note, the spreadsheet converts the entered value of $(R_{max} - R_{min})/R_{min}$ into the appropriate $2(R_{max} - R_{min})/(R_{max} + R_{min})$ for Eq. (3).

Bridge Parameters			**Resulting Circuit Values**					
Voltage Drop Each Junctio	1.00E-01	V	Supply Voltage		3.2			
MTJ's Per Leg	16							
Area of Each Junction	8000	um^2	Resistance per Junction		125.00	Ohms	kT	4.14E-021
			Current Through Each Leg		8.00E-004	A	gammaMs	1.77E+011
Operational Parameters			Power (All 4 Legs)		5.12E-03	W		
Free layer Saturation Field	3.00E-004	T	Sensitivity		8888.89	V/T		
TMR (enter: delta-R/R-min)	100	%	Free Layer Volume		8.00E-015	m^3		
Flux concentrator gain	5							
Amplifier Noise	1	nV/Hz$^{0.5}$	**Noise Analysis**					
Temperature	300	K	Voltage noise power		voltage noise		field noise	
Junction Resistance.Area	1.00E+00	MOhm.um^2	Amplifier Noise					
Ms	8.00E+005	A/m	1.00E-018	V^2/Hz	1.00E-009	V/Hz$^{0.5}$	1.13E-013	T/Hz$^{0.5}$
Damping alpha	0.01							
Electronic 1/f noise alpha	1.00E-009	um^2	Johnson/Shot					
Operating frequency	1.00E+04	Hz	coth arg	1.93E+000	Shot Dominated			
Free layer Thickness	1.00E+00	um	6.68E-017	V^2/Hz	8.17E-009	V/Hz$^{0.5}$	9.20E-013	T/Hz$^{0.5}$
Magnetic1/f noise alpha	1.83E-12	um3T						
Physical Constants			Electronic 1/f noise					
e	1.60E-019	A.s	2.00E-018	V^2/Hz	1.41E-009	V/Hz$^{0.5}$	1.59E-013	T/Hz$^{0.5}$
kB	1.38E-023	J/K						
Gamma	2.21E+005	mA^{-1}s^{-1}	Thermal Mag noise					
mu zero	1.26E-006	TmA^{-1}	2.84E-021	V^2/Hz	5.33E-011	V/Hz$^{0.5}$	9.59E-014	T/Hz$^{0.5}$
			Magnetic 1/f noise					
			5.30E-020	V2/Hz	2.30E-010	V/Hz0.5	4.14E-013	T/Hz0.5
					Total Noise Floor		1.03E-012	T/Hz$^{0.5}$

Written out explicitly,

$$S_B = \frac{4B_{sat}^2}{(\Delta R/\bar{R})^2 N^2 V_J^2} \times \left[S_V^{Amp} + N\frac{2eV_J[RAP]}{A}\coth\left(\frac{eV_J}{2k_BT}\right) + N\frac{\alpha_{elect.}V_J^2}{Af} \right] + \frac{1}{N}\frac{4k_BT\mu_0\alpha_G}{\Omega\gamma M_s} + \frac{2B_{sat}}{N}\frac{\alpha_{mag}}{\Omega f} \qquad (24)$$

3. Results and discussion

To characterize the expected performance of sensors the field noise (the square root of the field noise power) was studied as a function of the input variables for Eq. (24), using an Excel[1,2] spreadsheet for the calculation. Table 2 presents the starting point for this work. It assumes that reasonable values for the three key properties can be integrated into a sensor. For TMR a value of 100% is assumed, although values above 400% have been reported [13–15]. For the saturation field, $B_{sat,}$ of the free layer 3×10^{-4} T (3 Oe) was assumed, although values almost 100 times smaller have been demonstrated in magnetic thin films not incorporated in MTJs [16]. Incorporation of ultrasoft magnetic films in MTJs typically results in exposure to stray fields that raise B_{sat} significantly. For the magnetic flux concentrator a gain of 5 with an operating frequency of 10 kHz was used since these values have recently been demonstrated [6]. The resulting noise floor is 1 pT/rt(Hz).

A key point about the magnetic flux concentrator is that it acts to modulate the magnetic field. Thus, the magnetic sensor is operating in a higher frequency region where the $1/f$ noise is much lower. The signal appears as sidebands to the signal of the output voltage at the resonant frequency of the MEMS structure. The signal can be demodulated using a lock-in amplifier.

For other parameters, the assumptions were as follows:

1) A Wheatstone bridge with 16 MTJ sensors in each leg, a supply voltage of 3.2 V to hold the drop across each MTJ at 0.1 V.
2) Rather large junction areas of 8000 μm^2 and free-layer thicknesses of 1 μm to increase the volume and thereby reduce thermal magnetic noise.
3) A large RA product of 1 MΩ μm^2 to raise the resistance of the large-area MTJs, thereby limiting the current and holding the power consumption to 5 mW.
4) A saturation magnetization, M_s, corresponding to permalloy.
5) A typical Gilbert damping parameter of 0.01.
6) A electronic Hooge $1/f$ noise parameter of 1×10^{-9} μm^2 which is typical for the RA product value.
7) A typical magnetic Hooge $1/f$ noise parameter for MTJs of 1.83×10^{-12} μm^3 T.

The above key parameters and other enumerated parameters do not place any great demands on MTJ fabrication or performance. The challenge lies in integrating the components without significant loss of the performance demonstrated separately.

First, it is important to validate the theoretical model in Eq. (24). If the parameters for current commercial sensors are use in Eq. (24), the experimental results are predicted quite accurately. For example, Fig. 2 is adapted from Ref. [17] which published results on

[1] The identification of a commercial software is to specify the experimental methods and does not imply any NIST endorsement or recommendation that it is necessarily the best for the purpose.
[2] The identification of commercial sensors is to specify the experimental methods and does not imply any NIST endorsement or recommendation that they are necessarily the best for the purpose.

Table 3
A set of input parameters for Eq. (24) used to calculate the orange dot at 1 Hz in Fig. 2.

Bridge Parameters				**Resulting Circuit Values**						
Voltage Drop Each Junctio	1.00E-01	V		Supply Voltage		4				
MTJ's Per Leg	20									
Area of Each Junction	300	um^2		Resistance per Junction		3333.33	Ohms	kT	4.14E-021	J
				Current Through Each Leg		3.00E-005	A	gammaMs	1.77E+011	s^{-1}
Operational Parameters				Power (All 4 Legs)		2.40E-04	W			
Free layer Saturation Field	1.00E-003	T		Sensitivity		1666.67	V/T			
TMR (enter: delta-R/R-min)	40	%		Free Layer Volume		3.00E-018	m^3			
Flux concentrator gain	5									
Amplifier Noise	500	$nV/Hz^{0.5}$		**Noise Analysis**						
Temperature	300	K		Voltage noise power		voltage noise		field noise		
Junction Resistance.Area	1.00E+00	$MOhm.um^2$		Amplifier Noise						
Ms	8.00E+005	A/m		2.50E-013	V^2/Hz	5.00E-007	$V/Hz^{0.5}$	3.00E-010	$T/Hz^{0.5}$	
Damping alpha	0.01									
Electronic 1/f noise alpha	1.00E-008	um^2		Johnson/Shot						
Operating frequency	1.00E+00	Hz		coth arg	1.93E+000	Shot Dominated				
Free layer Thickness	1.00E-02	um		2.23E-015	V^2/Hz	4.72E-008	$V/Hz^{0.5}$	2.83E-011	$T/Hz^{0.5}$	
Magnetic1/f noise alpha	1.83E-12	um3T								
Physical Constants				Electronic 1/f noise						
e	1.60E-019	A.s		6.67E-012	V^2/Hz	2.58E-006	$V/Hz^{0.5}$	1.55E-009	$T/Hz^{0.5}$	
kB	1.38E-023	J/K								
Gamma	2.21E+005	$mA^{-1}s^{-1}$		Thermal Mag noise						
mu zero	1.26E-006	TmA^{-1}		1.36E-019	V^2/Hz	3.69E-010	$V/Hz^{0.5}$	4.43E-012	$T/Hz^{0.5}$	
				Magnetic 1/f noise						
				8.47E-014	V2/Hz	2.91E-007	V/Hz0.5	3.49E-009	T/Hz0.5	
						Total Noise Floor		3.83E-009	$T/Hz^{0.5}$	

several commercial sensors. Note Ref. [17] uses the term detectivity in the same sense we use total noise floor. The orange dots are the values we obtained using Eq. (24) for the sensor labeled NVE SDT, using appropriate values for the parameters of that sensor [18]. The agreement is excellent. Table 3 shows the spreadsheet values for 1 Hz.

Note that the 1 pT/rt(Hz) prediction in Table 2 above is frequency independent below 10 kHz because of the effect of the oscillation flux concentrator. Note also that 1 pT is a factor-of-ten below the abscissa in Fig. 2. The potential improvement in the type of sensors we analyze here is especially important for detecting low-frequency signals, with over a one-thousand-fold improvement, from 13 nT/rt(Hz) to 1 pT/rt(Hz), projected by Fig. 2 at 0.1 Hz, in agreement with the conclusions of Ref. [6]. The key factors in this huge improvement are the use of the oscillating MEMS flux concentrator and the large free-layer volume.

We have found the spreadsheet based on Eq. (24) to be a valuable tool for

1) providing quick evaluations of the effect of changing the sensor parameters,
2) formulating a best compromise solution to the inevitable trade-offs,
3) analysing existing sensors to see where improvements may be made,
4) gaining deeper insights into how existing sensors perform.

Fig. 3 presents the spreadsheet projections for the effect of changing the TMR. Clearly, there is not much gained by TMR values above 100%, while the losses below 50% become severe.

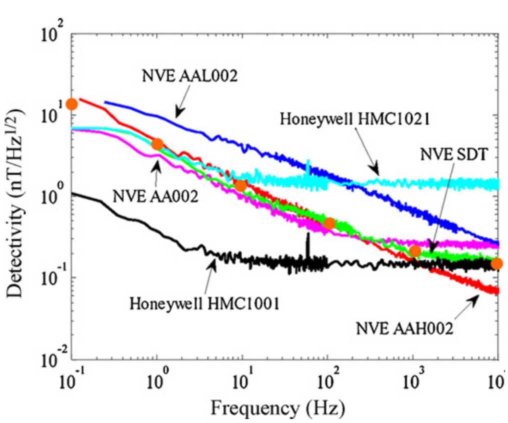

Fig. 2. An adaptation of a figure in Ref. [17] comparing the detectivity versus frequency for commercial sensors.* The orange dots are our results predicting the behavior of the NVE SDT sensor using Eq. (24). Ref. [17] uses the term detectivity in the same sense we use total noise floor. (For interpretation of the references to color in this figure legend, the reader is referred to the web version of the article.)

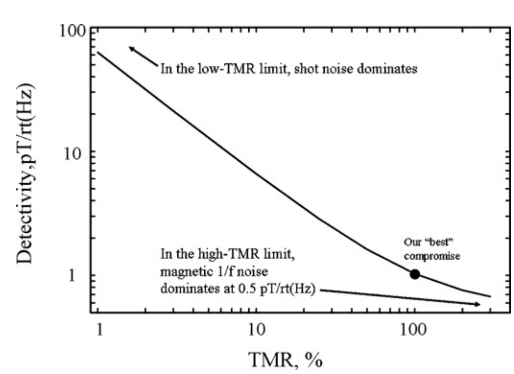

Fig. 3. The projection for the effect on detectivity of changing TMR when all other parameters are held at the "best compromise" values presented in Table 1. No frequency is specified for the detectivity since the MEMS flux concentrator should make it frequency independent below 10 kHz.

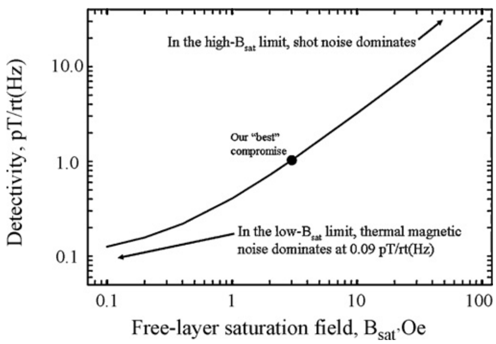

Fig. 4. The projection for the effect on detectivity of the saturation field of the free layer when all other parameters are held at the "best compromise" values presented in Table 1. No frequency is specified for the detectivity since the MEMS flux concentrator should make it frequency independent below 10 kHz.

Lessons such as this one are extremely valuable in finding the optimum allocation of available resources. Since the high-TMR limit is 0.5 pT/rt(Hz) which is only slightly below our 1 pT/rt(Hz) "best compromise", striving for TMR values significantly above 100% would be a poor appropriation of resources.

Fig. 4 presents the spreadsheet projections for the effect of changing B_{sat}, the free-layer saturation field. In this case, the low-B_{sat} limit for the detectivity is 0.09 pT/rt(Hz), but such values require an unrealistic B_{sat} of $\approx 10^{-6}$ T. Unfortunately, we have found experimentally that reducing B_{sat} below $\approx 10^{-4}$ T in MTJs is very challenging. Nevertheless, the payoff from reducing B_{sat} is significant, and an appropriation of resources might be productive in this area, particularly in the form of higher-gain flux concentrators. Our assumption of a gain of 5 is moderate. At least, we know from the spreadsheet projections that there is the potential for a large improvement in MTJ sensors by lowering B_{sat}.

In existing MTJ sensors, B_{sat} values tend to be in the range of 10^{-3} T or more. There are two primary difficulties in achieving such B_{sat} values. One is orange-peel coupling and the other is magnetization ripple.

Orange-peel coupling is a well-known problem in MTJs [19] and we have found ways to reduce its effect to the level of $\approx$0.1 mT (1 Oe) [20,21]. Magnetization ripple is less familiar and more difficult to deal with. It is illustrated in Fig. 5.

The image is recorded with scanning electron microscopy with polarization analysis (SEMPA) [22]. The sample is Si(1 0 0)\250 nm thermal oxide\10 nm IrMn\5 nm Co. The color wheel in the lower left corner indicates the direction of the local magnetization in the image. The arrow in the color wheel points in the yellow direction meaning that direction is the mean magnetization direction, M_{mean}. The green and red bands are magnetization ripple. They are caused by the polycrystalline IrMn grains having different preferred pinning axes. Exchange stiffness prevents the local magnetization from aligning perfectly with the pinning axis of each IrMn grain. The ripple bands are local minimum energy configurations that establish local magnetization directions to balance the energies from the exchange bias by the IrMn, the exchange stiffness of the Co, and the stray fields above and below the Co layer.

On the right side of Fig. 5 are plots of scans of the magnetization direction parallel and perpendicular to the mean magnetization direction, labeled Y and X respectively. In the upper part of the image, the line through the green band defines a k wavevector (2π/width of the band) for the green band and an angle φ which represents the difference between k and M_Y, the Y component of the magnetization. The Y component of the magnetization is the component parallel to the mean magnetization. The angle between the local magnetization direction and the mean magnetization is θ. Note that the two angles are not quite equal. The green bands all have the same magnetization direction, but their k wavevectors vary somewhat.

These terms may be used in the equation

$$H_{stray} \approx 4\pi M_s t_{Co} \sin\theta \frac{k}{2} \sin\varphi \qquad (25)$$

to provides an estimate of the stray field just above the pinned layer that the free layer will experience in an MTJ. In regions where the ripple bands are not pronounced, such as where the scans are made, this field is estimated to be on the order of 10^{-4} T (1 Oe) whereas where the bands are intense, as in the green band that defines k, it is estimated to be on the order of 17×10^{-4} T (17 Oe). The parameters used for the former estimate are the value of Co for $4\pi M_s$, $\varphi = 10°$, $\theta = 5°$, $k = 2\pi/1000$ nm, and $t_{Co} = 5$ nm. For the latter estimate, they are the value of Co for $4\pi M_s$, $\varphi = 40°$, $\theta = 30°$, $k = 2\pi/1000$ nm, and $t_{Co} = 5$ nm.

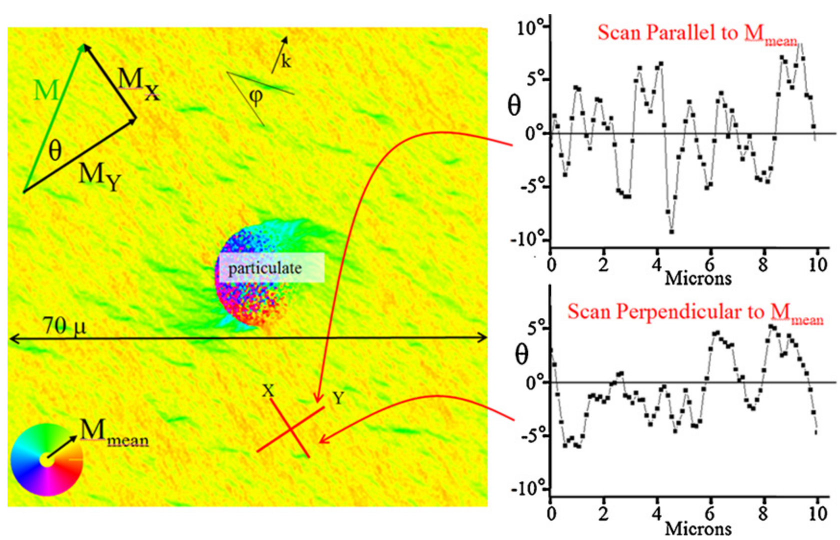

Fig. 5. An example of magnetization ripple in the Co film of a Si(1 0 0)\250 nm thermal oxide\10 nm IrMn\5 nm Co structure. The particulate on the surface is not relevant. It simply facilitates focusing the electron beam. Plots of θ, the angle between the local magnetization direction and the mean magnetization direction (shown in the color wheel), are given for scans in the directions X and Y. X is parallel to the mean magnetization direction and Y is perpendicular to it. (For interpretation of the references to color in this figure legend, the reader is referred to the web version of the article.)

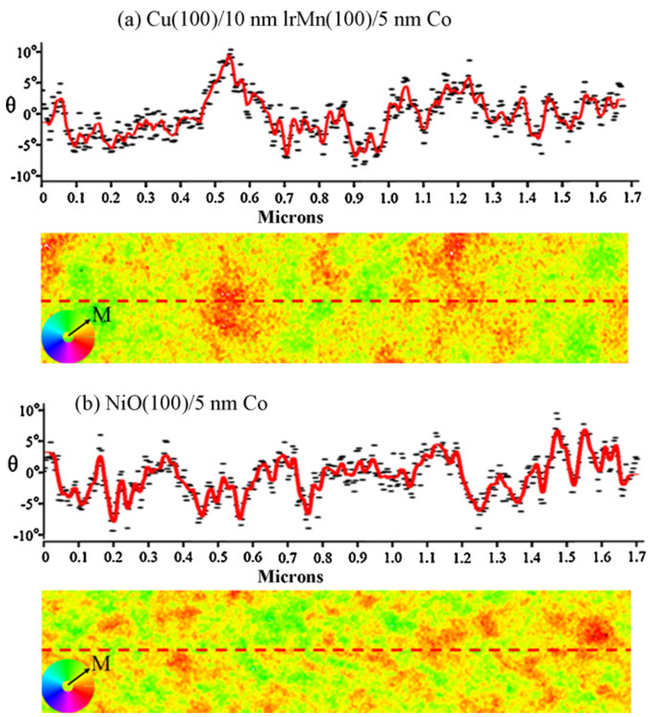

Fig. 6. Plots of θ, the angle between the local magnetization direction and the mean magnetization direction, and the corresponding real space SEMPA images for a) Cu(1 0 0)\10 nm IrMn(1 0 0)\5 nm Co and b) NiO(1 0 0)\5 nm Co. The dashed red lines are the path of the plotted scan. (For interpretation of the references to color in this figure legend, the reader is referred to the web version of the article.)

Eq. (25) may be readily understood on the basis of simple magnetostatics. For any local area, the maximum stray field it can create is $M_X \approx 4\pi M_s t_{Co} \sin\theta$. However, if it is present in a band for which $\varphi = 0^\circ$ there are no free poles to create a stray field. If $\varphi = 90^\circ$, the maximum stray field is present. This effect has the functional form $(k/2)\sin\varphi$.

Eq. (25) and Fig. 5 indicate that the stray fields emanating from the magnetization ripple caused by polycrystalline IrMn may be a serious problem in making major reductions in B_{sat}. Some approaches to the problem that are likely to help are the use of synthetic antiferromagnets in pinned layers to give partial cancellation of stray fields and thinner layers of IrMn to weaken the strength of the pinning. However, one possibility that does not appear to have been investigated is the use of single-crystal pinning layers. We have investigated two types of single-crystal pinning layers by SEMPA. One is NiO(1 0 0) grown epitaxially on MgO(1 0 0). The other is IrMn(1 0 0) grown epitaxially on Cu(1 0 0). In both cases, low energy electron diffraction (LEED) was used to confirm the epitaxial growth.

Fig. 6 presents the SEMPA results of 5 nm Co films on these two single-crystal substrates. Clearly, magnetization ripple is not eliminated by single-crystal pinning layers. However, there are major differences. The length scale of the magnetization ripple is about an order of magnitude smaller in Fig. 6 than it is in Fig. 5. This effect is likely the result of the single-crystal pinning layer having little or no contribution to the ripple, with the residual ripple caused by magnetocrystalline anisotropy in the Co. LEED indicates that Co does not grow epitaxially on either of these substrates.

The effect the reduced length scale is to increase k and thus the stray field according to Eq. (25). Also, the bands of Fig. 5 have become patches in Fig. 6, increasing the stray field by tending to eliminate the $(k/2)\sin\varphi$ term in Eq. (25). Additional work will be needed to determine the net effect of these two influences on B_{sat} of the free layers in MTJs, but the initial prognosis is not favorable for Co. Fortunately, alloys with nearly zero magnetocrystalline anisotropy should solve the problem.

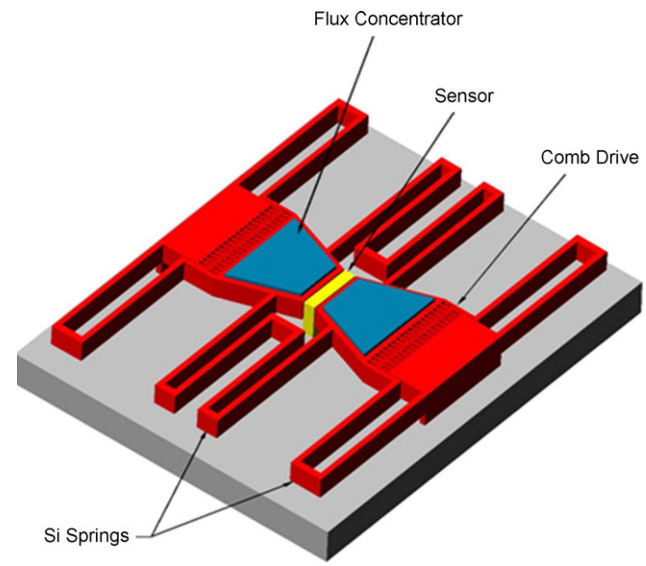

Fig. 7. An illustration of the oscillating MEMS flux concentrator that may solve the problem of low-frequency 1/*f* noise in magnetic sensors by shifting the signal to 10 kHz [6].

The use of a MEMS magnetic flux concentrator is critical to achieving high sensitivity at low frequency. It acts to modulate the magnetic field so even a very low-frequency magnetic signal is detected at the oscillating frequency of flux concentrator. As a result, the magnetic sensor is operating in a high frequency region where the 1/*f* noise is much lower. The signal appears as sidebands to the signal of the output voltage at the resonant frequency of the MEMS structure. The signal can be demodulated using a lock-in amplifier. Fig. 7 is an illustration of the device.

Fig. 8 presents the spreadsheet projections for the effect of changing the operating frequency of the MEMS magnetic flux concentrator when all other parameters are held at the "best compromise" values presented in Table 1. The flux concentrator would probably not operate at frequencies below 1 kHz, however values lower than that in Fig. 8 correspond to the detectivity at those frequencies in the absence of an oscillating flux concentrator. Clearly, operating the oscillating flux concentrator at 10 kHz gives orders of magnitude of improvement for frequencies below 1 Hz [6]. Fig. 8 indicates, as seen in Figs. 3 and 4, there is little to be gained by going beyond our "best compromise" value. Shot and amplifier noise are not reduced by using higher frequencies, and they set a noise floor.

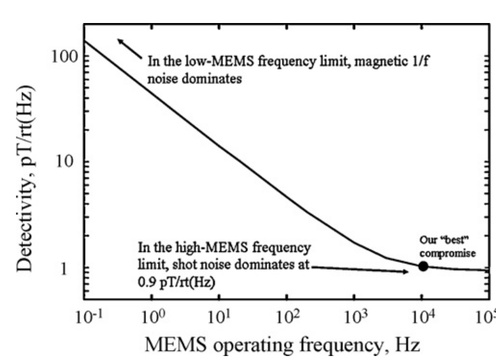

Fig. 8. The projections for the effect on detectivity of the frequency of operation of the MEMS flux concentrator when all other parameters are held at the "best compromise" values presented in Table 1.

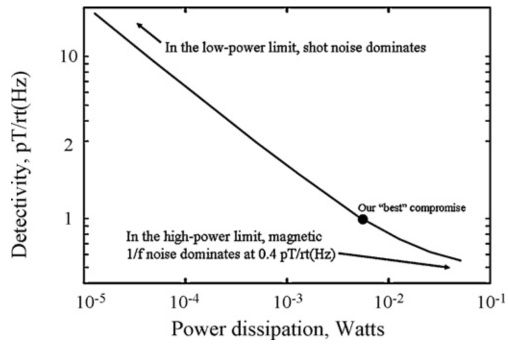

Fig. 9. The projections for the power dissipation requirement of the Wheatstone bridge for achieving levels of detectivity (by varying RA) when all other parameters are held at the "best compromise" values presented in Table 1.

Recently, a different design of a MEMS flux concentrator based on a torsional cantilever was published [23]. The detection of a static field of 2.7 μT was reported, and improvements are likely as the design efficiency develops.

Fig. 9 presents the spreadsheet projections for the effect of changing the power dissipation (by varying RA) when all other parameters are held at the "best compromise" values presented in Table 1. For applications in which minimizing the power consumption is an important issue, it may be noted that the spreadsheet projects that if the power consumption is reduced to 1 mW the detectivity increases to 2 pT/rt(Hz). Note that this is the power requirement for the Wheatstone bridge and does not include the power for the amplifier which will require a few additional milli-Watts depending on the application.

For real-world applications, one of the principle considerations will be thermal drift in the control electronics. Thermal drift must be slow on the scale of the frequency of the signal the sensor is attempting be measured. Our preliminary estimates are that to detect 1 pT/rt(Hz), the drift must be less than 0.01 °C per cycle. For example, to observe a signal at 0.1 Hz, the drift must be less than 0.001 °C/s. Clearly, thermal insulation of the sensor, perhaps incorporating a thermal bath for stabilization, will help to enable the detection of signals at the lowest frequencies.

4. Conclusions

The major conclusions of this work may be summarized as follows:

1) Recent advances in TMR, free-layer saturation field, and MEMS oscillating flux concentrators suggest that it may be possible to use small, inexpensive, low-power, ultra-sensitive magnetic sensors to detect 1 pT/rt(Hz) at low frequencies, a regime which is currently dominated by fluxgates, optically pumped magnetometers and SQUIDS.
2) The major challenge is to integrate these advances into sensors with only moderate loss in the separately demonstrated levels of performance.
3) If successful, these sensors will play important roles in a wide range of applications including healthcare, homeland security, and national defense.

Acknowledgements

One of us (ASE) would like to acknowledge valuable discussions on MEMS flux concentrators with Neil Smith (then) of IBM. E.R.N. acknowledges support from ONR under STTR award N00014-07-C-0355 and DOE under award DE-FG02-07ER46374. The authors would like to acknowledge valuable assistance and discussions on various aspects of this work with: Roger Koch, Neil Smith (HGST), Bill Doyle, Mark Stiles, Brian Maranville, Moshe Schmoueli, Cindi Dennis, Mike Donahue, Casey Uhlig, John Bonevich, Dave Pappas, Steve Russek, Tom Silva, Mike Donahue, Justin Shaw, P.J. Chen, and Audie Castillo.

References

[1] http://www.newswiretoday.com/news/9947/.
[2] A. Baschirotto, F. Borghetti, E. Dallago, P. Malcovati, M. Marchesi, E. Melissano, P. Siciliano, G. Venchi, Fluxgate magnetic sensor and front-end circuitry in an integrated microsystem, Sens. Actuators 132 (2006) 90.
[3] http://www.prc68.com/I/Sensors.shtml#MEG.
[4] NIST Magnetic Sensors Roadmap (2003), See: http://qdev.boulder.nist.gov/817.03/whatwedo/magsensors/Roadmap.doc;.
[5] N. Smith, A.M. Zeltser, D.L. Yang, P.V. Koeppe, Very high sensitivity GMR spin-valve magnetometer, IEEE Trans. Mag. 33 (1997) 3385; N. Smith, L. Kunstmanus, private communication on modulation.
[6] A.S. Edelstein, G.A. Fischer, M. Pedersen, E.R. Nowak, Shu Fan Cheng, C.A. Nordman, Progress toward a thousand-fold reduction in 1/f noise in magnetic sensors using an AC MEMS flux concentrator, J. Appl. Phys. 99 (2006) 08B317.
[7] (a) E.R. Nowak, M.B. Weissman, S.S.P. Parkin, Electrical noise in hysteretic ferromagnet–insulator–ferromagnet tunnel junctions, Appl. Phys. Lett. 74 (1999) 600;
(b) J.M. Almeida, R. Ferreira, P.P. Freitas, J. Langer, B. Ocker, W. Maass, 1/f noise in linearized low resistance MgO magnetic tunnel junctions, J. Appl. Phys. 99 (2006) 08B314;
(c) R.C. Chaves, P.P. Freitas, B. Ocker, W. Maass, Low frequency picoTesla field detection using hybrid MgO based tunnel sensors, Appl. Phys. Lett. 91 (2007) 102504;
(d) R.C. Chaves, P.P. Freitas, B. Ocker, W. Maass, MgO based picoTesla field sensors, J. Appl. Phys. 103 (2008) 07E931.
[8] (a) L. Jiang, E.R. Nowak, P.E. Scott, J. Johnson, J.M. Slaughter, J.J. Sun, R.W. Dave, Low-frequency magnetic and resistance noise in magnetic tunnel junctions, Phys. Rev. B 69 (2004) 054407;
(b) A. Ozbay, A. Gokce, T. Flanagan, R.A. Stearrett, E.R. Nowak, C. Nordman, Low frequency magnetoresistive noise in spin-valve structures, Appl. Phys. Lett. 94 (2009) 023502.
[9] (a) N. Smith, P. Arnett, White-noise magnetization fluctuations in magnetoresistive heads, Appl. Phys. Lett. 78 (2001) 1448;
(b) N. Smith, P. Arnett, Thermal magnetization noise in spin valves, IEEE Trans. Mag. 38 (2002) 32.
[10] S.H. Liou, R. Zhang, S.E. Russek, L. Yuan, S.T. Halloran, D.P. Pappas, Dependence of noise in magnetic tunnel junction sensors on annealing field and temperature, J. Appl. Phys. 103 (2008) 07E920.
[11] (a) H.T. Hardner, M.B. Weissman, M.B. Salamon, S.S.P. Parkin, Fluctuation-dissipation relation for giant magnetoresistive 1/f noise, Phys. Rev. B 48 (1993) 16156;
(b) S. Ingvarsson, G. Xiao, S.S.P. Parkin, W.J. Gallagher, G. Grinstein, R.H. Koch, Low-frequency magnetic noise in micron-scale magnetic tunnel junctions, Phys. Rev. Lett. 85 (2000) 3289;
(c) L. Jiang, E.R. Nowak, P.E. Scott, J. Johnson, J.M. Slaughter, J.J. Sun, R.W. Dave, Low-frequency magnetic and resistance noise in magnetic tunnel junctions, Phys. Rev. B 69 (2004) 054407;
(d) C. Ren, X. Liu, B.D. Schrag, G. Xiao, Low-frequency magnetic noise in magnetic tunnel junctions, Phys. Rev. B 69 (2004) 104405;
(e) D. Mazumdar, X. Liu, B.D. Schrag, W. Shen, M. Carter, G. Xiao, Thermal Stability, sensitivity, and noise characteristics of MgO-based magnetic tunnel junctions, J. Appl. Phys. 101 (2007) 09B502;
(f) D. Mazumdar, X. Liu, B.D. Schrag, M. Carter, W. Shen, G. Xiao, Low frequency noise in highly sensitive magnetic tunnel junctions with (001) MgO barrier, Appl. Phys. Lett. 91 (2007) 033507.
[12] A. Ozbay, A. Gokce, T. Flanagan, R.A. Stearrett, E.R. Nowak, C. Nordman, Low frequency magnetoresistive noise in spin-valve structures, Appl. Phys. Lett. 94 (2009) 023502.
[13] Y. Lee, J. Hayakawa, S. Ikeda, F. Matsukura, H. Ohno, Effect of electrode composition on the tunnel magnetoresistance of pseudo-spin-valve magnetic tunnel junction with a MgO tunnel barrier, Appl. Phys. Lett. 90 (2007) 212507.
[14] S. Yuasa, A. Fukushima, H. Kubota, Y. Suzuki, K. Ando, Giant tunneling magnetoresistance up to 410% at room temperature in fully epitaxial Co/MgO/Co magnetic tunnel junctions with bcc Co(001) electrodes, Appl. Phys. Lett. 89 (2006) 042505.
[15] J. Hayakawa, S. Ikeda, Y.M. Lee, F. Matsukura, H. Ohno, Effect of high annealing temperature on giant tunnel magnetoresistance ratio of CoFeB/MgO/CoFeB magnetic tunnel junctions, Appl. Phys. Lett. 89 (2006) 232510.
[16] W.F. Egelhoff Jr., R.D. McMichael, C.L. Dennis, M.D. Stiles, F. Johnson, A.J. Shapiro, B.B. Maranville, C.J. Powell, Soft magnetic layers for low-field-detection magnetic sensors, Thin Solid Films 505 (2006) 90.
[17] N.A. Stutzke, S.E. Russek, D.P. Pappas, M. Tondra, Low-frequency noise measurements on commercial magnetoresistive magnetic field sensors, J. Appl. Phys. 97 (2005) 10Q107.
[18] M. Tondra, personal communication.

[19] B.D. Schrag, A. Anguelouch, S. Invarsson, G. Xiao, Y. Lu, P.L. Trouilloud, A. Gupta, R.A. Wanner, W.J. Gallagher, P.M. Rice, S.S.P. Parkin, Néel "orange-peel" coupling in magnetic tunneling junction devices, Appl. Phys. Lett. 77 (2000) 2373.
[20] W.F. Egelhoff Jr., R.D. McMichael, C.L. Dennis, M.D. Stiles, A.J. Shapiro, B.B. Maranville, C.J. Powell, Suppression of orange-peel coupling in magnetic tunnel junctions by preoxidation, Appl. Phys. Lett. 88 (2006) 162508.
[21] W.F. Egelhoff Jr., R.D. McMichael, C.L. Dennis, M.D. Stiles, A.J. Shapiro, B.B. Maranville, C.J. Powell, Preoxidation as a general approach to suppressing orange-peel coupling in magnetic tunnel junctions, IEEE Trans. Mag. 42 (2006) 2664.
[22] http://physics.nist.gov/Divisions/Div841/Gp3/Facilities/sempa.html.
[23] A. Guedes, S. Patil, S. Cardoso, V. Chu, J.P. Conde, P.P. Freitas, Hybrid magnetoresistive/microelectromechanical devices for static field modulation and sensor 1/*f* noise cancellation, J. Appl. Phys. 103 (2008) 07E924.

Biographies

W.F. Egelhoff, Jr. is a NIST Fellow at the National Institute of Standards and Technology. He received a PhD in physical chemistry from the University of Cambridge in 1975, he was a postdoc at Caltech 1976–1977, he was a researcher at the GM Labs 1977–1979, and he has been at NIST since 1979. His primary work has been in surface and interfacial effects in thin-film magnetism, magnetoresistance effects (Ballistic, Giant, Anisotropic, & Tunneling), magnetic sensors, ultra-high-density data storage media, surfactants in thin-film growth, specular electron scattering in thin films, oscillatory exchange coupling, photoelectron diffraction including semi-classical electron-atom scattering models, and core-level binding-energy shifts.

P.W.T. Pong is a physicist and electrical engineer working on magnetoresistive magnetic field sensors and cancer nanotechnology at the Department of Electrical and Electronic Engineering (EEE), University of Hong Kong (HKU). He received a PhD in engineering from the University of Cambridge in 2005. After working as a post-doctoral researcher at the Magnetic Materials Group at the National Institute of Standards and Technology (NIST) for three years, he joined the HKU engineering faculty where he is now an assistant professor working on magnetic-tunnel-junction (MTJ) sensors, and the application of nanotechnology in cancer research.

J. Unguris is a physicist working on nanomagnetism at the National Institute of Standards and Technology (NIST). He received a PhD from the University of Wisconsin in 1980. After a two year National Research Council (NRC) postdoctoral fellowship, he joined the permanent staff at NIST where he initially worked on developing new electron spin sensitive measurements and spectroscopies. His current work focuses on using Scanning Electron Microscopy with Polarization Analysis (SEMPA) to image the nanoscale magnetic structure of magneto-electronic devices and materials.

R.D. McMichael is a physicist working on nanomagnetics at the Center for Nanoscale Science and Technology at the National Institute of Standards and Technology (NIST). He received a PhD in physics from the Ohio State University in 1990. After a National Research Council postdoctoral research associateship at NIST he joined the NIST staff in 1992 where he has worked on a broad range of magnetic topics including magnetocaloric effect, hysteresis modeling, ferromagnetic resonance, giant magnetoresistance, and micromagnetic modeling. His current research focuses on magnetic property measurements at thin-film edges and spin-torque effects in ferromagnetic resonance.

E.R. Nowak is an associate professor in the Department of Physics and Astronomy at the University of Delaware. He received a PhD in physics from the University of Minnesota in 1994 and held postdoctoral appointments at The University of Chicago and The University of Illinois at Urbana-Champaign. He has worked in the fields of high-T_c superconductivity, spin electronics, and dense granular media. His current interests involve using noise and fluctuations as a probe of electronic and magnetic properties spin-based magnetoresistive materials and devices. He also serves as editor of the journal, *Fluctuation and Noise Letters*.

A.S. Edelstein is a physicist working as team leader for a group working on improving and using magnetic sensors at the Army Research Lab at Adelphi, MD. He received his PhD at Stanford University in 1963. He has worked previously at IBM, University of Illinois, and NRL. He has worked on Nanomaterials and magnetic moment formation in Ce based alloys and compounds. The latter included studies of concentrated Kondo system, mixed valence systems, and heavy fermion systems.

James E. Burnette is a physicist working on the development of radiometric sensors at the U.S. Army Research Laboratory. He received his bachelor of science degree from Morehouse College in 1993, majoring in physics. In 1995 he received his master of science degree in physics from Clark-Atlanta University, where his thesis research focused on mathematical modeling of biological systems. In 2004, he received is PhD in physics from North Carolina State University, where his thesis research was focused on the growth and characterization of semiconductor thin films. In 2006, he received a postdoctoral position at the U.S. Army Research Laboratory as an Oak Ridge Associated Universities Fellow. His current research interests include flexible displays, flexible electronics, and biomimetics.

Greg Fischer was born in California, USA, in 1964. He received his bachelor of science in physics at the University of California, San Diego (UCSD) in 1988. From there he went to San Diego State University and worked on high temperature superconductor research, receiving his master of science in physics in 1992. He then returned to UCSD and entered the Materials Science Program. He pursued research on magnetic recording media at the Center for Magnetic Recording Research and received his PhD in materials science in 2000. He received a postdoctoral position at the US Army Research Laboratory in that same year from the American Society for Engineering Education and was subsequently hired on as a Materials Scientist. His fields of interest included magnetic sensors, magnetic recording media, read heads, magnetic modeling, and superconductivity.